crystals

MDPI

Article

Stability of $FeVO_4$-II under Pressure: A First-Principles Study

Pricila Betbirai Romero-Vázquez [1], Sinhué López-Moreno [2,3,*] and Daniel Errandonea [4]

1 División de Materiales Avanzados, IPICYT, Camino a la presa de San José 2055 Col. Lomas 4a sección, San Luis Potosí 78126, Mexico
2 CONACYT—División de Materiales Avanzados, IPICYT, Camino a la presa de San José 2055 Col. Lomas 4a sección, San Luis Potosí 78126, Mexico
3 Centro Nacional de Supercómputo, IPICYT, Camino a la presa de San José 2055 Col. Lomas 4a sección, San Luis Potosí 78126, Mexico
4 Departamento de Física Aplicada, Instituto de Ciencias de Materiales, MALTA Consolider Team, Universidad de Valencia, 46100 Valencia, Spain
* Correspondence: sinhue.lopez@ipicyt.edu.mx

Abstract: In this work, we report first-principles calculations to study $FeVO_4$ in the $CrVO_4$-type (phase **II**) structure under pressure. Total-energy calculations were performed in order to analyze the structural parameters, the electronic, elastic, mechanical, and vibrational properties of $FeVO_4$-**II** up to 9.6 GPa for the first time. We found a good agreement in the structural parameters with the experimental results available in the literature. The electronic structure analysis was complemented with results obtained from the Laplacian of the charge density at the bond critical points within the Quantum Theory of Atoms in Molecules methodology. Our findings from the elastic, mechanic, and vibrational properties were correlated to determine the elastic and dynamic stability of $FeVO_4$-**II** under pressure. Calculations suggest that beyond the maximum pressure covered by our study, this phase could undergo a phase transition to a wolframite-type structure, such as in $CrVO_4$ and $InVO_4$.

Keywords: $FeVO_4$ under pressure; $CrVO_4$-type structure; first-principles; mechanical properties; vibrational properties; electronic properties

check for updates

Citation: Romero-Vázquez, P. B.; López-Moreno, S.; Errandonea, D. Stability of $FeVO_4$-II under Pressure: A First-Principles Study. *Crystals* **2022**, *12*, 1835. https://doi.org/10.3390/cryst12121835

Academic Editor: Artem R. Oganov

Received: 18 November 2022
Accepted: 13 December 2022
Published: 15 December 2022

1. Introduction

High-pressure studies on ABO_4 compounds have increased in the last two decades due to the evolution of the diamond-anvil cell (DAC) and its impact on other relevant areas, such as materials sciences [1,2]. Among ABO_4 compounds, those with a $CrVO_4$-type structure (Space Group, SG, *Cmcm*, No. 63, $Z = 4$, with [6 − 4] coordination for the [*A*-*B* cations]) have received less attention. $CrVO_4$-type compounds are a family formed mainly by phosphates, vanadates, chromates, and sulfates [3]. Given their position in the Bastide diagram [4], it has been reported that they could have a structural phase transition driven by pressure to the wolframite [5,6] or zircon [7,8] structure. This implies a change in the coordination to [6 − 4 + 2] and [8 − 4] in the high-pressure phases, respectively.

According to the literature, AVO_4 vanadates with $CrVO_4$-type structures have been used in applications as photocatalyst materials [1,9,10], cathodoluminescent materials [11,12], and scintillators [13,14], among others. The properties of these compounds are reported to be highly dependent on the occupation of the *d* valence electrons of the transition metal cations [9–14]. Until now, only four vanadates with a $CrVO_4$-type structure have been reported: $CrVO_4$ [6], $FeVO_4$ [15], $InVO_4$ [16], and the less studied $TlVO_4$ [3]. Unlike the other vanadates, $FeVO_4$ presents a great polymorphism, crystallizing at ambient conditions in the triclinic $AlVO_4$-type [17] structure (SG: $P\bar{1}$, No. 2, $Z = 6$) [15], while the $CrVO_4$-type phase was obtained from high-pressure-high-temperature studies [18] and synthesized at ambient conditions by hydrothermal method [19]. Further, the antiferromagnetic order in $FeVO_4$-**II** was observed after the characterization of its magnetic properties [19]. However, until now, no more experimental or theoretical studies have been reported to characterize this phase. It

is worth mentioning that most of the studies carried out at high pressure on this compound have focused on characterizing the crystal structure of the different polymorphs [15,18,20–22].

In this work, we performed a first-principles characterization of $FeVO_4$-**II** up to 9.6 GPa. The main goal is to determine the elastic and dynamic stability of the studied polymorph at ambient conditions and under pressure. In this sense, a complete report of the elastic constants, mechanical properties, elastic anisotropy, and vibrational properties is presented. Furthermore, given the relevance of the electronic structure of this compound in materials science, we computed the density of states and the band structure together with an analysis of the charge density with the QTAIM methodology [23,24].

2. Computational Details

Total energy calculations were performed within the framework of the density functional theory (DFT) [25] and the projector-augmented wave (PAW) [26,27] method as implemented in the Vienna *Ab initio* Simulation Package (VASP) [28–31]. We used a plane-wave energy cutoff of 520 eV to ensure high precision in our calculations. The exchange-correlation energy was described within the generalized gradient approximation (GGA) in the Perdew–Burke–Ernzerhof for solids (PBEsol) formulation [32]. The GGA+U was used to account for the strong correlation between the electrons in the d shell, on the basis of Dudarev's method [33]. In this method, the Coulomb interaction U and the onsite exchange interaction J_H are treated together as $U_{eff} = U - J_H$. For our GGA+U calculations, we choose U = 6 eV and J_H = 0.95 eV. Similar values were previously used with relative success in the study of other iron and vanadate compounds [15,20,34–37].

The Monkhorst-Pack scheme was employed for the Brillouin-zone (BZ) integrations [38] with a mesh 4 × 3 × 3, which corresponds to a set of 8 special k-points in the irreducible BZ. In the relaxed equilibrium configuration, the forces are less than 0.3 meV/Å per atom in each Cartesian direction. The highly converged results on forces are required for the calculations of the dynamical matrix using the direct force constant approach [39], which allows us to identify the irreducible representation and the character of the phonon modes at the zone center (Γ point). The phonon density of states (PDOS) were obtained from the calculation of the phonons in the whole BZ with a supercell 2 × 2 × 2 times the conventional unit cell by using the PHONON software. The calculations of elastic constants were made following the methodology validated in Ref. [40] with a k-points mesh of 8 × 6 × 6, a plane-wave energy cutoff of 570 eV, and a POTIM parameter of 0.016. The elastic tensor is determined by performing six finite distortions of the lattice and deriving the elastic constants from the strain–stress relationship [41]. The electron density was computed with a refined grid to be analyzed within the fundaments of Quantum Theory of Atoms in Molecules (QTAIM) [42] with CRITIC [43,44], and AIM [45] codes.

3. Results and Discussion

3.1. Crystal Structure

According to the literature, $FeVO_4$ has been successfully synthesized as a metastable polymorph at ambient conditions in the orthorhombic $CrVO_4$-type structure (SG: *Cmcm*, No. 63, Z = 4) [19], also called the $FeVO_4$-**II** phase, see Figure 1a. In this structure, there are four non-equivalent Wyckoff positions (WP): Fe occupies the 4*a* (0, 0, 0), V the 4*c* (0, y, 1/4), and O the 8*f* (0, y, z), and 8*g* (x, y, 1/4). Internally, the structure consists of edge-sharing FeO_6 distorted octahedra along the c direction. The –FeO_6–FeO_6– chains are linked together by means of the VO_4 distorted tetrahedra, while the VO_4 tetrahedra are not linked to each other, as can be seen in Figure 1b. As shown in Figure 1c, there are two non-equivalent interatomic distances in the FeO_6 octahedra, the apical Fe-O distance (d_{Fe-O1}) and the equatorial Fe-O distance (d_{Fe-O2}). In the VO_4 tetrahedra, there are two V–O interatomic distances (d_{V-O1} and d_{V-O2}). In both polyhedra, the respective interatomic distance d_{X-O2} is larger than d_{X-O1} (X = Fe, V). Inside the polyhedrons, there are important angles to mention that are relevant for the structural changes in the polyhedra under pressure. The α

angle is formed between the equatorial plane of the FeO_6 octahedra and the polar bond, while the β (γ) angle is between the two d_1 (d_2) interatomic distances of the VO_4 tetrahedra.

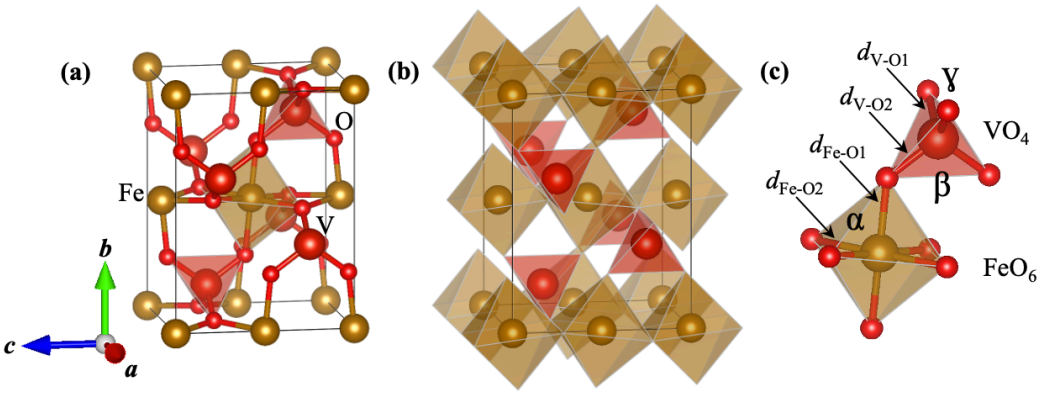

Figure 1. (**a**) Crystal structure of $FeVO_4$-**II** polymporph, (**b**) polyhedral representation of the structure, and (**c**) irregular polyhedra of FeO_6 and VO_4 units. The different bond distances mentioned in the text are labeled as well as the bond angles. We used the VESTA software [46] to build the structures.

The equilibrium volume and unit-cell parameters at $P \approx 0$ GPa were computed by minimizing the total crystal energy for different volumes ranging from -4 to 10 GPa while allowing the internal atomic positions and the lattice parameters to relax. We used the third-order Birch–Murnaghan [47] equation-of-state (EOS) to fit the volume–energy curve. Our results showed that the lowest energy configuration is obtained when an antiferromagnetic coupling between Fe ions is obtained, in accordance with the experimental results from Mössbauer effect [19]. The optimized lattice parameters (a, b, c), volume (V), interatomic distances (d_{Fe-O1}, d_{Fe-O2}, d_{V-O1}, d_{V-O2}), internal angles (α, β, γ), bulk modulus (B) and pressure derivative of B (B') appear in Table 1 together with experimental results from the literature [19]. Furthermore, we have included the reported parameters for other $CrVO_4$-type structure vanadates for comparison. According to Table 1, the equilibrium volume at ambient pressure of AVO_4 (A = Cr, Fe, In, Tl) compounds increases with the atomic mass of cation A, while the opposite occurs for bulk modulus. The obtained results for $FeVO_4$–**II** are in excellent agreement with experiments, with a difference of less than 1% in the lattice parameters. For this volume, the WPs are 4a (0, 0, 0) for Fe, 4c (0, 0.35788, 1/4) for V, 8f (0, 0.76239, 0.96753), and 8g (0.26481, 0.47778, 1/4) for O. Following Table 1, the equilibrium volume at ambient pressure of AVO_4 (A = Cr, Fe, In, Tl) compounds increases with the atomic mass of cation A. In contrast, the opposite occurs for bulk modulus.

Table 1. Calculated structural parameters for $FeVO_4$-**II** phase. a, b, and c are the lattice parameters, V is the volume, d_{X-On} (X = Fe, V; n = 1, 2) and α, β, and γ, are the interatomic distances and angles inside the crystal structure, respectively (see Figure 1). B is the bulk modulus and B' is the pressure derivative of B. Results from this work are denoted with $\star$. We also include experimental results from the literature of AVO_4 compounds for comparison.

	a (Å)	b (Å)	c (Å)	V (Å^3)	d_{Fe-O1} (Å)	d_{Fe-O2} (Å)	d_{V-O1} (Å)	d_{V-O2} (Å)	α (°)	β (°)	γ (°)	B (GPa)	B'	Ref.
$FeVO_4$	5.6038	8.2624	6.1726	285.80	1.9734	2.0377	1.6705	1.7842	89.271	106.990	112.547	88.8	2.8	$\star$
	5.5941	8.3216	6.2252	289.80	1.9784	2.0521	1.6544	1.7762				88.3	3.2	DFT [15]
	5.6284	8.2724	6.1118	284.57	2.0060	2.0290	1.6520	1.7920	89.600	107.200	112.500			Exp. [19]
$CrVO_4$	5.5785	8.2830	6.0576	279.90								93.0	4.0	DFT [6]
	5.5680	8.2080	5.9770	273.16								63.0	4.0	Exp. [6]
$InVO_4$	5.7547	8.6168	6.6751	331.00	2.1877	2.1392	1.6690	1.7824				71.0	4.0	DFT [5]
	5.7380	8.4920	6.5820	320.72								69.0	4.0	Exp. [16]
$TlVO_4$	5.8390	8.6870	6.8000	344.92										Exp. [48]

According to the most recent high-pressure experiments carried out on $FeVO_4$ [15,20], this compound undergoes the following phase transition sequence, $P\bar{1} \rightarrow P\bar{1}' \rightarrow \alpha$-$MnMoO_4$-type, driven by pressure. However, previous high-pressure studies reported

the next phase transition sequence $P\bar{1} \rightarrow$ $CrVO_4$-type $\rightarrow$ wolframite in a small range of pressure [49]. Therefore, it is unknown if the $CrVO_4$-type structure of $FeVO_4$ would transition to wolframite when high-pressure experiments are carried out starting from the $CrVO_4$-type structure, as occurs with $CrVO_4$ [6] and $InVO_4$ [5,16], and was predicted through first-principles calculations [15]. Therefore, from now on, we will only deal with studying the behavior of $FeVO_4$-**II** under pressure without considering whether the $CrVO_4 \rightarrow$ wolframite transition occurs. Figure 2 shows the pressure evolution of the structural parameters for the $FeVO_4$-**II** phase. According to Figure 2a, a volume reduction of $\Delta V = -9$ % is observed for a range of pressure of ≈10 GPa. Considering the anisotropy of the orthorhombic crystal structure, ΔV is more reflected in the [010] and [001] directions, while the change in [100] is practically negligible, see Figure 2b. Indeed the compressibility of the [001] direction is comparable to the linear compressibility of diamond, making the studied material a near zero linear compressibility material along [001]. The anisotropy can also be understood with the help of the other internal parameters from Figure 2c–f. As seen in Figure 2c, the interatomic distances d_{Fe-On} of FeO_6 undergo more changes than the d_{V-On} distances of VO_4, which is reflected in the larger compressibility of V_{FeO_4} octahedra against the minimal change in V_{VO_4}, see Figure 2d. Hence, the large compressibility of the *y*-axis is due primarily to the compressibility of octahedra due to the reduction in d_{Fe-O2}. Whereas, despite the reduction in d_{V-O2}, the β and γ angles adjust in such a way that V_{VO_4} remains almost constant with pressure. On the other hand, the distortion parameter Δ_d presents an important change at 6.2 GPa, which will be discussed in detail in Section 3.3.

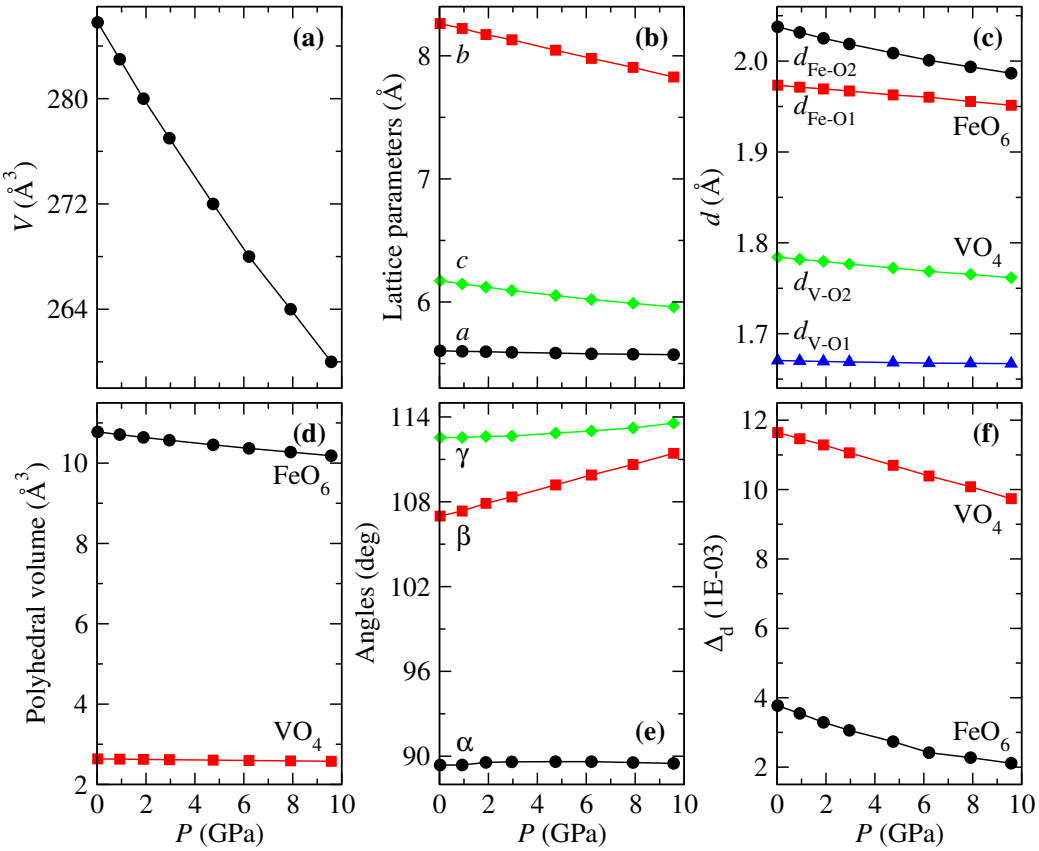

Figure 2. Structural parameters for $FeVO_4$-**II** as a function of pressure: (**a**) volume, (**b**) lattice parameters, (**c**) interatomic distances, (**d**) polyhedral volumes, (**e**) angles, and (**f**) polyhedral distortion parameter.

3.2. Electronic Structure

Figure 3a,b displays our calculated density of states (DOS) and band structures along the high-symmetry path Z–Γ–S–R–Z–T–Y–Γ of the $FeVO_4$-**II** phase at ambient pressure and 9.6 GPa, respectively. Red dashed lines at 0 eV indicate the Fermi level. At ambient

pressure, the valence band maximum (VBM) is located at an H ($\frac{1}{2}$, $\frac{1}{2}$, $-u$) point (between T and Y), mainly occupied by $2p$ (p_x) states from oxygen. In contrast, the conduction band minima (CBM) is located at the Γ point with contributions of the $3d$ states from Fe, mostly from d_{yz} sub-orbital. Therefore, $FeVO_4$-**II** phase presents an indirect energy band-gap E_g = 2.11 eV. In comparison, the direct Γ–Γ energy band-gap is 2.17 eV. In this case, the maximum at Γ below the Fermi level is occupied by $2p$ (p_x and p_y) states from oxygen, as happens in other ABO_4 compounds [40]. It has been reported that CBM of many rare-earth AVO_4 vanadates is dominated by vanadium $3d$ states, which makes these compounds present energy band-gaps close to 3.8 eV [50,51]. However, in the case of vanadates $InVO_4$ (phase **II**), $CrVO_4$ (phase **II**), and $FeVO_4$ (phase **I**), the energy band-gap lowers to 3.2, 2.6, and 2.1 eV, respectively, due to contribution from cation A to the valence and conduction band [5,6,50,52]. Hence, our E_g value follows the observed results for those vanadates. According to partial electronic DOS of Figure 3a, the states below the Fermi level mainly belong to the O atoms. In contrast, the states above the conduction bands are due to Fe, followed by V and O.

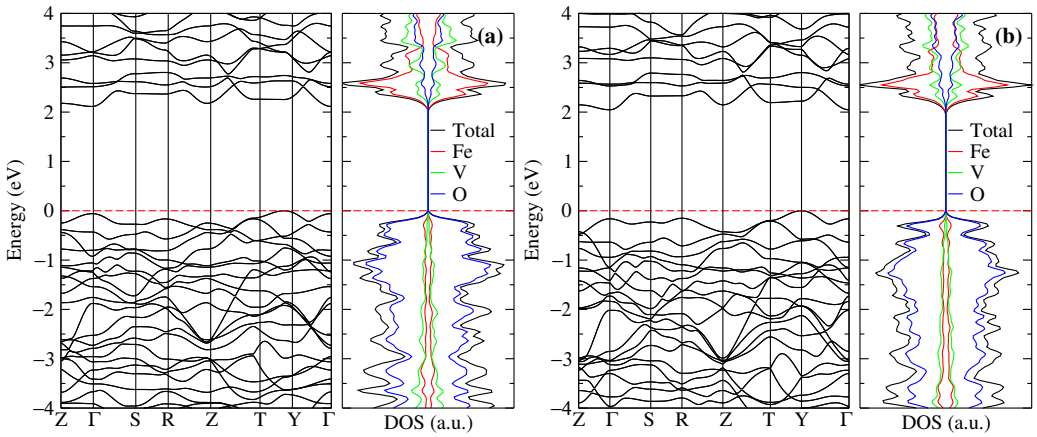

Figure 3. Band structure and electronic density of states at (**a**) ambient pressure and (**b**) 9.6 GPa of $FeVO_4$-**II** phase.

As pressure increases up to 9.6 GPa, the VBM shifts to the high-symmetry point Y while the CBM is still at the Γ point with the same band occupation observed at ambient pressure, see Figure 3b. Hence, at this pressure, the band-gap is still indirect with E_g = 2.05 eV, which gives a pressure coefficient of $dE_g/dp = -7.1$ meV/GPa. In contrast, the pressure coefficients for $InVO_4$ and $CrVO_4$ are positive, with values of 13.5 [52] (8.9 [5]) meV for $InVO_4$ and 1.9 (4.1) meV for $CrVO_4$ [6], obtained by optical absorption measurements (DFT calculations). On the other hand, the forbidden direct Γ–Γ band-gap increases with pressure up to 2.21 eV at 9.6 GPa, which gives a value of dE_g/dP = 4.2 meV, similar to the obtained values for the other AVO_4 vanadates.

We performed a topological analysis of the charge density (ρ) with the QTAIM methodology to complement the study of the electronic structure of $FeVO_4$-**II**. Figure 4a,b show the gradient vector field of the electron density ($\nabla\rho$) of FeO_6 and VO_4 polyhedra, respectively (gold for Fe, purple for V, and red for O). Blue points indicate the atomic nucleus, corresponding to the maximum critical points (MCP). The minimal CP (mCP) are in green, and the bond CPs (BCPs) are in black and are located in the bond path (blue dashed lines) between Fe (V) and O. The distance between Fe (V) and the BCP (d_{BCP}) is plotted as a function of pressure in Figure 4c. As seen, the distances d_{BCP} follow the same trend observed in the interatomic distances of Figure 2c. Therefore, the crystal structure can be interpreted in terms of charge density. In this sense, the Laplacian of the charge density ($\nabla^2\rho_{BCP}$) at the BCP gives an idea of the ionicity ($\nabla^2\rho_{BCP} > 0$) or covalency ($\nabla^2\rho_{BCP} < 0$) of a system [53]. According to Figure 4d, the Fe–O and V–O bonds have an ionic nature. The obtained values of $\nabla^2\rho_{BCP}$ (0.214–0.295 a.u.) for Fe–O bonds in the distorted octahedra are larger than those reported for A–O bonds in AWO_4 (0.086–0.147 a.u.) [54], $AMoO_4$ (0.085–0.22 a.u.) [53], and

$ATcO_4$ (0.045–0.153 a.u.) [40] compounds. In the case of the VO_4 distorted tetrahedra, there is a significative difference in the values of $\nabla^2\rho_{BCP_1}$ and $\nabla^2\rho_{BCP_2}$, which is related to the interatomic distances d_{V-On} (see Table 1) being significantly larger than those obtained for the FeO_6 distorted octahedra. This is the reason for the low compressibility of the VO_4 polyhedra. As the pressure grows, the Laplacian values increase, strengthening the Fe–O and V–O bonds and the resistance of the polyhedrons to compression.

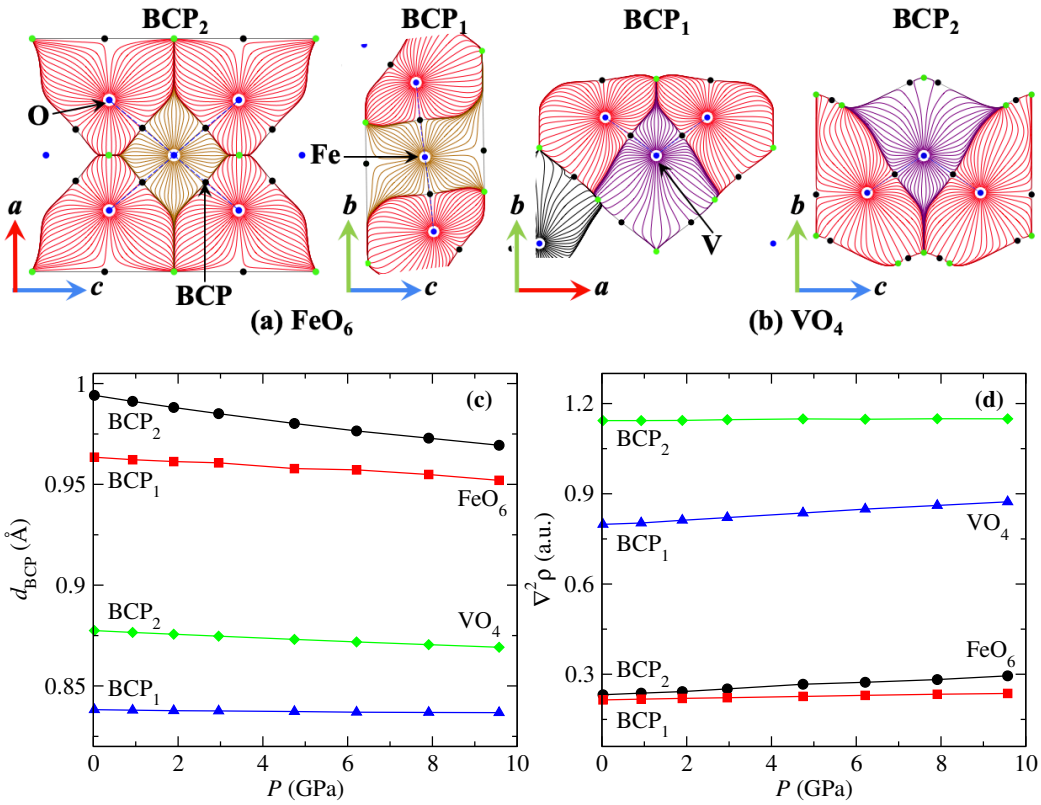

Figure 4. Gradient vector field of the electron density ($\nabla\rho$) for (**a**) FeO_6 and (**b**) VO_4 polyhedra. (**c**) Evolution of the interatomic distances from the cations to the critical bond points and (**d**) Laplacian of the charge density at the critical bond point as a function of pressure for $FeVO_4$.

3.3. Elastic constants and mechanical properties

The elastic constants (c_{ij}) determine the resistance to deformation in the directions and planes of a crystal, making them highly dependent on the system's symmetry. For the orthorhombic crystalline system, there are nine independent elastic constants: c_{11}, c_{22} and c_{33} for longitudinal compression, c_{12}, c_{13} and c_{23} for transverse expansion, c_{44}, c_{55}, and c_{66} for pure shear [55]. Table 2 shows the elastic constants c_{ij} of $FeVO_4$-**II** at 0 GPa and the respective pressure coefficients dc_{ij}/dP. The necessary and sufficient Born stability criteria for orthorhombic systems are [56]: $c_{11} > 0$, $c_{11}c_{22} > c_{12}^2$, $c_{11}c_{22}c_{33} + 2c_{12}c_{13}c_{33} + 2c_{12}c_{13}c_{23} - c_{11}c_{23}^2 - c_{22}c_{13}^2 - c_{33}c_{12}^2 > 0$, $c_{44} > 0$, $c_{55} > 0$, and $c_{66} > 0$, which are fulfilled for $FeVO_4$-**II**. Under hydrostatic pressure (P), the stability criteria are [57]: $c_{ii} - P > 0$ (i = 1 to 6), $c_{11} + c_{22} + c_{33} + 2c_{12} + 2c_{13} + 2c_{23} + 3P > 0$, $c_{11} + c_{22} - 2c_{12} - 4P > 0$, $c_{11} + c_{33} - 2c_{13} - 4P > 0$, and $c_{22} + c_{33} - 2c_{23} - 4P > 0$, which are also meet. According to Table 2, the elastic constant c_{11} presents the higher value, followed by c_{33} and c_{22}, indicating that longitudinally the crystal is more resistant to deformation in the a-axis; this was also observed in the evolution of the lattice parameters under pressure in Figure 2b. As would be expected, the largest transverse expansion constant is c_{12}, followed by c_{13} and c_{23}, c_{33} being the smallest of the nine elastic constants. At the same time, the shear elastic constants are generally small against those from longitudinal compression and transverse expansion. We found that elastic constants follow a linear trend with pressure, where only c_{22} presents

a negative pressure coefficient related to the trends observed in the structural parameters with pressure.

Table 2. Elastic constants c_{ij} (in GPa) at 0 GPa and pressure coefficients.

	c_{11}	c_{22}	c_{33}	c_{44}	c_{55}	c_{66}	c_{12}	c_{13}	c_{23}
c_{ij}	234.2	125.5	144.8	62.98	52.49	47.04	78.46	68.21	39.81
dc_{ij}/dP	2.41	−0.87	3.78	0.74	1.04	0.15	2.39	2.18	2.57

The elastic constants and compliances were used to compute the bulk (B) and shear (G) modulus with the Hill procedure [58], which is the average of the Voigt (V) [59] and Reuss (R) [60] methods. The bulk modulus in the Voigt and Reuss methods is computed as follows: $9B_V = (c_{11} + c_{22} + c_{33} + 2c_{12} + 2c_{13} + 2c_{23})$, and $B_R^{-1} = (s_{11} + s_{22} + s_{33} + 2s_{12} + 2s_{13} + 2s_{23})$, respectively. While the shear modulus is obtained with the following equations: $15G_V = (c_{11} + c_{22} + c_{33} - c_{12} - c_{23} - c_{13} + 3c_{44} + 3c_{55} + 3c_{66})$, and $15G_R^{-1} = [4(s_{11} + s_{22} + s_{33}) - 4(s_{12} + s_{13} + s_{23}) + 3(s_{44} + s_{55} + s_{66})]$, respectively. B and G in the Hill average are obtained by means of $B = (B_V + B_R)/2$ and $G = (G_V + G_R)/2$, respectively. On the other hand, Young's modulus (E) and Poisson's ratio (ν) are given by $E = 9BG/(3B + G)$ and $\nu = (3B - 2G)/(6B + 2G)$, respectively. The Vickers hardness was calculated with the approximation of Tian et al. [61]: $H_v = 0.92\, k^{1.137} G^{0.708}$, $k = G/B$.

The mechanical properties and their evolution with pressure are provided in Figure 5. As seen, B increases almost linearly with pressure, which means that the resistance to deformation increases for this pressure range. Whereas G undergoes a change in the linear trend above 3 GPa, reaching a maximum value of 53.9 at 6.2 GPa and falling down to 53.3 GPa at 9.6 GPa. There is no significant change in G for this pressure range, but the change in trend will substantially affect the other properties that depend on G. Interestingly, in other materials, such change in the slope of the pressure dependence of the shear modulus G has been identified as a precursor effect of a phase transition observed at higher pressures [62]. According to the equations of Voigt and Reuss for G, the behavior of G is due to the negative pressure coefficient for c_{22} and the significant values of dc_{ij}/dP for the transverse expansion elastic constants. On the other hand, B behaves linearly because B_V (B_G) only sums the longitudinal and transverse elastic constants (compliances), while c_{22} (s_{22}) decreases with pressure, so the value of c_{22} affects B by a small constant factor.

The behavior of Young's modulus is similar to G due to its relation with this mechanical property. According to Figure 5c, E increases by 4.3 % in a pressure range of 7.86 GPa; above this pressure, it decreases from 138.1 to 137.6 GPa. This behavior indicates that $FeVO_4$ could undergo a phase transition from a $CrVO_4$-type phase to another one at a relatively small pressure since it has been observed that $FeVO_4$ undergoes several phase transitions below 10 GPa, see Refs. [15,20] and references therein. The Poisson's ratio follows an increasing trend, taking values between 0.26 and 0.29, which are in the range for ceramic semiconductors (0.25–0.42) [63] and are similar for other ABO_4 compounds [40,54,64]. These values indicate that ionic contribution dominates in $FeVO_4$-**II**. The Pugh relation, Figure 5e, represents the ductility or brittleness of the system. A value below 1.75 [11] reveals a tendency to brittleness, while a value greater than this indicates that the material behaves in a ductile manner. $FeVO_4$-**II** presents a value of 1.745 at ambient pressure and increases to 2.06 at 9.6 GPa, which means that ductility increases with pressure. As was expected, $FeVO_4$-**II**, as other ABO_4 compounds, presents a small Vickers hardness due to the relatively small values of B and G. Given the relation between H_V and B/G, it is natural that the Vickers hardness decreases with pressure, Figure 5f.

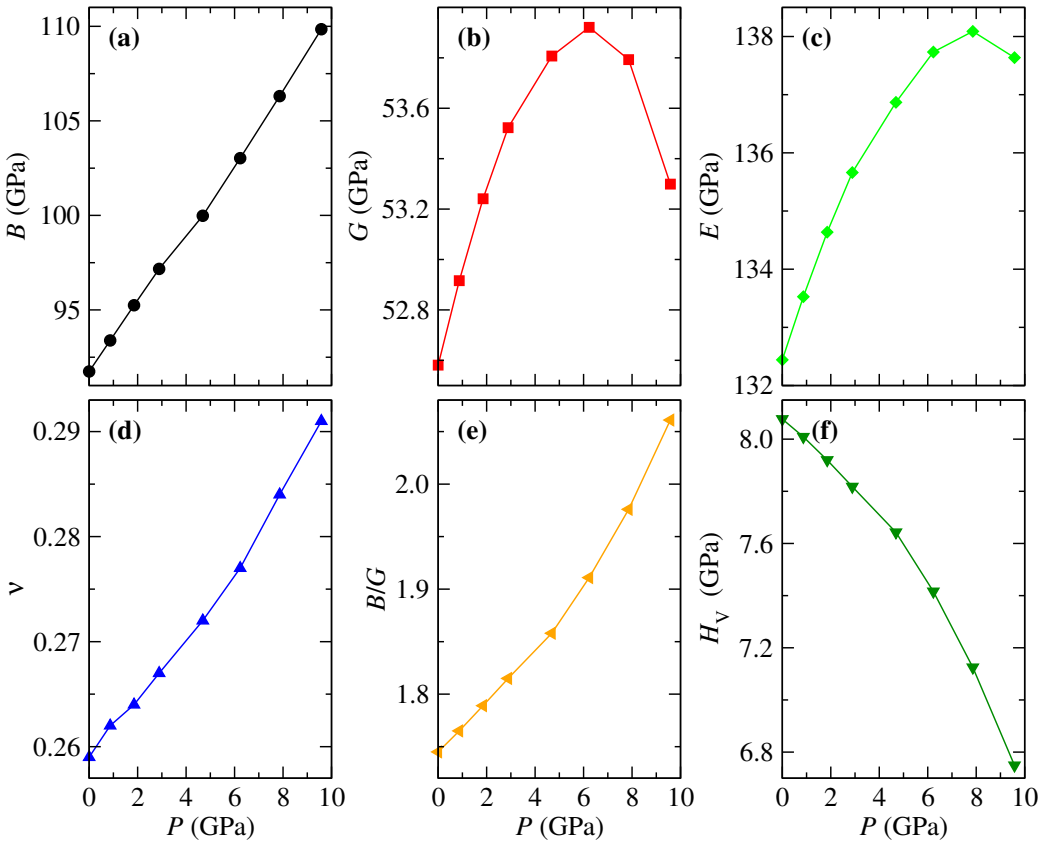

Figure 5. Pressure dependence of mechanical properties obtained from elastic constants with the Hill average: (**a**) bulk modulus, B, (**b**) shear modulus, G, (**c**) Young's modulus, E, (**d**) Poisson's ratio, ν, (**e**) Pugh's ratio, B/G, and (**f**) Vickers hardness, H_V, for $FeVO_4$-**II**.

On the other hand, elastic anisotropy has important implications in engineering science and crystal physics because it is commonly responsible for the formation of microcracks in materials [65]. In this work, we analyzed several anisotropic factors discussed below. The anisotropic shear factors provide a measure of the degree of anisotropy in the bonding between atoms in different crystallographic planes. The shear anisotropic factor for the {100} shear planes between the ⟨011⟩ and ⟨010⟩ directions is $A_{\{100\}} = 4c_{44}/(c_{11} + c_{33} - 2c_{13})$. For the {010} shear planes between ⟨101⟩ and ⟨001⟩ directions it is $A_{\{010\}} = 4c_{55}/(c_{22} + c_{33} - 2c_{23})$. For the {001} shear planes between ⟨110⟩ and ⟨010⟩ directions, it is $A_{\{001\}} = 4c_{66}/(c_{11} + c_{22} - 2c_{12})$. The factors $A_{\{100\}}$, $A_{\{010\}}$, and $A_{\{001\}}$ must be one for isotropic crystals, and any value greater or smaller than one measures the degree of elastic anisotropy. According to Figure 6a, $A_{\{100\}}$ presents the smallest deviation from one, followed by $A_{\{010\}}$ and $A_{\{001\}}$. However, once pressure is applied, $A_{\{010\}}$ is more affected than the others. Factor $A_{\{010\}}$ is related to the equatorial interatomic distances of the distorted octahedra [d_{Fe-O2}, see Figure 2c], which makes quite a bit of sense since it is d_{Fe-O2} that undergoes the greatest change with pressure. While $A_{\{001\}}$ is more related to d_{Fe-O1}, with this interatomic distance being the second one most affected by pressure.

Other important factors are the universal anisotropy $A_U = 5G_V/G_R + B_V/B_R - 6$, the percentage of elastic anisotropy in bulk [$A_B = (B_V - B_R)/(B_V + B_R)$] and shear [$A_G = (G_V - G_R)/(G_V + G_R)$] modulus, where a value of zero is associated with isotropic elastic constants, which means that $B_V = B_R$ and $G_V = G_R$. For the entire range of pressure, A_B is larger than A_G because the difference between B_V and B_R is bigger than between G_V and G_R. However, the pressure affects more A_G than A_B as happens with G. This difference increases above 6.2 GPa as G_R presents the same behavior of G, while G_V is always increasing. A_U is larger than A_G and A_B since the anisotropies of both modules are added.

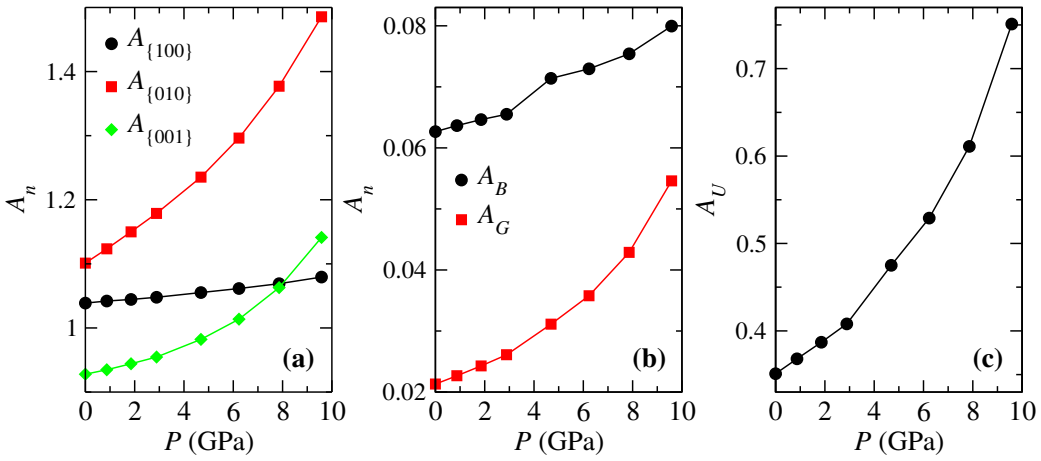

Figure 6. (**a**) Pressure dependence of anisotropy factors: (**a**) by crystallographic direction, (**b**) percentage bulk and shear anisotropy, and (**c**) universal anisotropy for $FeVO_4$-**II**.

3.4. Vibrational Properties

According to the group theory, the space group *Cmcm* has the following Raman, infrared (IR), and silent phonon modes at the zone center $\Gamma = 5A_g + 4B_{1g} + 2B_{2g} + 4B_{3g}$, $\Gamma = 6B_{1u} + 7B_{2u} + 5B_{3u}$, and $\Gamma = 3A_u$, respectively. These modes can be further classified into internal (symmetric stretching, ν_1, symmetric bending, ν_2, asymmetric stretching, ν_3, and asymmetric bending, ν_4) and external (translational, T, and rotational, R) modes of VO_4 units. The calculated Raman, IR, and silent phonon frequencies, the pressure coefficients ($d\omega/dP$), and the Grüneisen parameters (γ = -$\partial\ln(\omega)/\partial\ln V$) at the Γ point appear in Table 3.

Table 3. Calculated Raman, infrared, and silent phonon frequencies (ω in cm^{-1}), pressure coefficients ($d\omega/dp$), and Grüneisen parameters (γ) of $FeVO_4$-**II**.

	Raman				Infrared				Silent		
Mode	ω	$d\omega/dp$	γ	**Mode**	ω	$d\omega/dp$	γ	**Mode**	ω	$d\omega/dp$	γ
$T(B_{3g})$	153.7	1.37	0.57	$T(B_{1u})$	153.7	0.24	0.15	$T(A_u)$	164.4	1.29	0.77
$T(B_{1g})$	177.4	−1.05	−0.82	$T(B_{1u})$	180.8	1.68	0.86	$\nu_2(A_u)$	220.3	0.55	0.23
$R(B_{1g})$	219.6	0.52	0.22	$R(B_{3u})$	201.2	−0.01	−0.03	$\nu_2(A_u)$	404.9	7.45	1.68
$T(A_g)$	221.8	3.23	1.29	$\nu_2(B_{2u})$	274.9	1.12	0.37				
$R(B_{2g})$	261.8	4.25	1.47	$\nu_4(B_{3u})$	298.8	1.51	0.46				
$\nu_2(A_g)$	355.1	0.30	0.07	$T(B_{3u})$	315.1	3.82	0.25				
$\nu_4(B_{3g})$	361.7	1.36	0.33	$\nu_4(B_{2u})$	327.9	−0.88	−1.06				
$\nu_2(B_{2g})$	366.4	3.78	0.94	$R(B_{1u})$	363.1	2.41	0.48				
$\nu_4(B_{1g})$	374.0	3.58	0.88	$\nu_4(B_{2u})$	381.5	6.61	1.61				
$\nu_4(A_g)$	394.2	1.55	0.36	$\nu_4(B_{1u})$	398.3	4.93	1.13				
$\nu_4(B_{3g})$	431.3	5.90	1.25	$\nu_2(B_{2u})$	420.6	4.38	0.92				
$\nu_3(B_{1g})$	652.8	5.71	0.78	$\nu_3(B_{3u})$	654.2	5.64	0.77				
$\nu_3(A_g)$	751.0	5.74	0.72	$\nu_3(B_{2u})$	735.8	5.47	0.67				
$\nu_1(A_g)$	918.9	1.33	0.12	$\nu_3(B_{1u})$	866.8	2.58	0.26				
$\nu_3(B_{3g})$	922.0	2.44	0.24	$\nu_3(B_{2u})$	924.3	1.38	0.13				

According to Table 3, one Raman, $R(B_{1g})$, and two IR modes, $R(B_{3u})$ and $\nu_4(B_{2u})$, have negative pressure coefficients and Grüneisen parameters (soften with pressure), which are related to the instability of the $CrVO_4$-type structure under pressure [2]. Such behavior was already observed in $InVO_4$ [5] and $CrVO_4$ [20]. The soft translational Raman $T(B_{1g})$ mode involves a translation of the VO_4 polyhedra accompanied by a rotation of the FeO_6 units around the *z*-axis as rigid units, see Figure 7, whose freedom of movement is affected by the decrease in the lattice parameter *b*, which is the most compressible under pressure. In contrast, the remaining Raman modes harden with pressure. The IR soft $R(B_{3u})$ mode is quite similar to the $R(B_{1g})$, but in this case, the FeO_6 vibrates asymmetrically. While the other soft B_{2u} mode implies the asymmetric bending in the VO_4 polyhedra with a translation of the Fe cation in the *c* direction, which produces a stretching of the apical d_{Fe-O1} interatomic distances. Therefore, the softening of R and IR modes is related to the compression of the *y*-axis. Interestingly, phosphates with $CrVO_4$-type structure, such

as $InPO_4$ and $TiPO_4$, only present some IR soft modes. The main difference being that Ti(In)PO_4 is more compressible in the $c(b)$-axis [7].

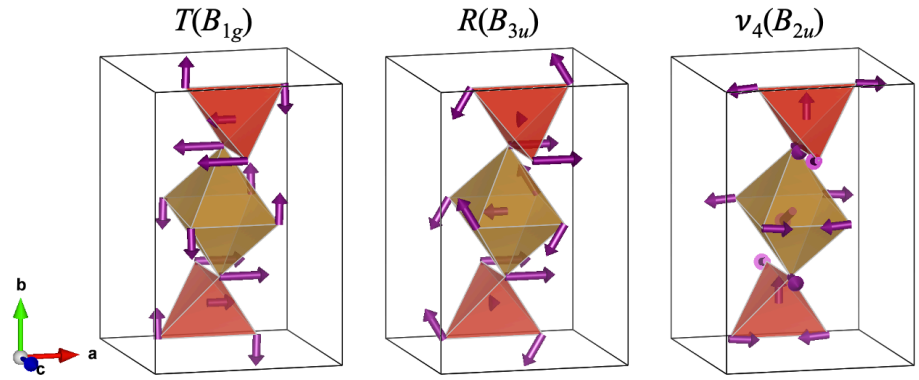

Figure 7. Eigenvectors of the phonon frequencies with negative pressure coefficients of $FeVO_4$-**II**. We used the VESTA software [46] to build the structures.

The phonon dispersion relation and the phonon density of states (DOS) are displayed in Figure 8 at (a) ambient pressure and (b) 9.6 GPa. As can be seen in Figure 8a, the $CrVO_4$-type structure of $FeVO_4$ complains with the dynamic stability criteria at $P = 0$, which implies that ω^2 (**q**, s)> 0 for all wave vectors **q** and polarization s (longitudinal and transverse modes) [66]. Therefore, $FeVO_4$-**II** complains with the elastic and dynamic stability criteria to be experimentally synthesized [19], such as $InVO_4$ [5] and $CrVO_4$ [20]. We can see no significant differences in the phonon spectrum at 9.6 GPa, which ensures that the $FeVO_4$-**II** phase would be stable in a pressure range where the isostructural vanadates $InVO_4$ and $CrVO_4$ undergo a phase transition to the wolframite-type structure [5,20].

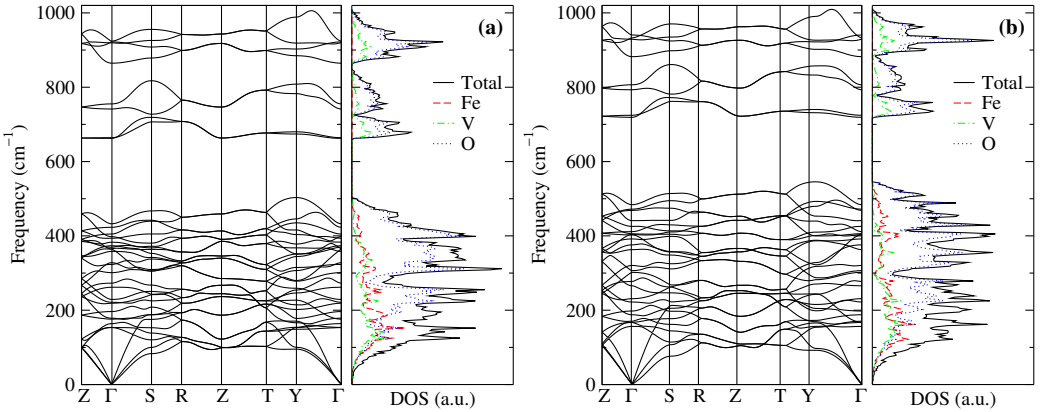

Figure 8. Phonon spectrum and phonon DOS at (**a**) 0 GPa, and (**b**) 9.6 GPa of $FeVO_4$-**II**.

The phonon DOS of $FeVO_4$-**II** is more similar to $CrVO_4$ than $InVO_4$ because In is more than double the mass of Cr and Fe. The partial phonon DOS of the first lower frequency zone (up to $\approx$ 505 cm^{-1}) is due to external (R and T) and internal (ν_2 and ν_4) phonon modes, with Fe and V similar contributions. In contrast, the two high-frequency zones are due to pure internal vibrations ν_1 and ν_3, which indicates that phonon DOS is only due to O and V.

4. Conclusions

First-principles calculations were performed to study $FeVO_4$ in the $CrVO_4$-type structure up to 9.6 GPa. Our results indicate that this phase is elastically and dynamically stable for this pressure range. $FeVO_4$ presents an indirect band-gap E_g = 2.11 eV, similar to the value reported for the triclinic phase of $FeVO_4$ at ambient pressure. The Laplacian charge density at BCPs in both polyhedra is larger than those reported for $AMoO_4$ and

AWO_4 compounds and increases with pressure. It was observed that the *y*-axis is the most compressible, related to the reduction in the interatomic distances of the FeO_6 polyhedra. These changes in the structural parameters have strong effects on the phonon modes with negative pressure coefficients. We found that the shear modulus *G* softens with pressure, which suggests that the $FeVO_4$-**II** phase could undergo a phase transition below 10 GPa as was predicted in a previous study and happen in $CrVO_4$ and $InVO_4$, where these compounds have a phase transition from $CrVO_4$-type to the wolframite structure. We hope this work encourages other research groups to perform high-pressure characterization studies with the diamond-anvil cell device in order to increase the knowledge of less studied orthovanadates with $CrVO_4$-type structure, such as $FeVO_4$ and $TlVO_4$.

Author Contributions: Methodology, P.B.R.-V., S.L.-M.; calculations, P.B.R.-V., S.L.-M.; writing—original draft preparation, P.B.R.-V., S.L.-M.; supervision, S.L.-M.; discussion, S.L.-M., D.E.; writing—review and editing, P.B.R.-V., S.L.-M., D.E. All authors have read and agreed to the published version of the manuscript.

Funding: S.L.-M. thanks CONACYT of Mexico for financial support through the program "Programa de Investigadoras e Investigadores por México". D.E. thanks the financial support from the Spanish Ministerio de Ciencia e Investigación (10.13039/501100011033) under Project PID2019-106383GB-41, as well as through the MALTA Consolider Team research network (RED2018-102612-T) and from Generalitat Valenciana under Grants PROMETEO CIPROM/2021/075-GREENMAT and MFA/2022/007.

Institutional Review Board Statement: Not applicable.

Informed Consent Statement: Not applicable.

Data Availability Statement: All relevant data that support the findings of this study are available from the corresponding authors upon request.

Acknowledgments: The authors gratefully acknowledge the computing time granted by LANCAD and CONACYT on the supercomputer Miztli at LSVP DGTIC UNAM. Furthermore, the IPICYT Supercomputing National Center for Education and Research, grant TKII-R2022-SLM1/PBRV1.

Conflicts of Interest: The authors declare no conflict of interest.

References

1. Errandonea, D.; Manjon, F. Pressure effects on the structural and electronic properties of ABX_4 scintillating crystals. *Prog. Mater. Sci.* **2008**, *53*, 711–773. [CrossRef]
2. Errandonea, D.; Garg, A.B. Recent progress on the characterization of the high-pressure behaviour of AVO_4 orthovanadates. *Prog. Mater. Sci.* **2018**, *97*, 123–169. [CrossRef]
3. Baran, E. Materials belonging to the $CrVO_4$ structure type: Preparation, crystal chemistry and physicochemical properties. *J. Mater. Sci.* **1998**, *33*, 2479–2497. [CrossRef]
4. de Jesus Pereira, A.L.; Santamaría-Pérez, D.; Vilaplana, R.; Errandonea, D.; Popescu, C.; da Silva, E.L.; Sans, J.A.; Rodríguez-Carvajal, J.; Muñoz, A.; Rodríguez-Hernández, P.; et al. Experimental and Theoretical Study of $SbPO_4$ under Compression. *Inorg. Chem.* **2020**, *59*, 287–307. [CrossRef] [PubMed]
5. López-Moreno, S.; Rodríguez-Hernández, P.; Munoz, A.; Errandonea, D. First-principles study of $InVO_4$ under pressure: phase transitions from $CrVO_4$-to $AgMnO_4$-type structure. *Inorg. Chem.* **2017**, *56*, 2697–2711. [CrossRef]
6. Botella, P.; López-Moreno, S.; Errandonea, D.; Manjón, F.J.; Sans, J.; Vie, D.; Vomiero, A. High-pressure characterization of multifunctional $CrVO_4$. *J. Phys. Condens. Matter.* **2020**, *32*, 385403. [CrossRef]
7. López-Moreno, S.; Errandonea, D. Ab initio prediction of pressure-induced structural phase transitions of $CrVO_4$-type orthophosphates. *Phys. Rev. B* **2012**, *86*, 104112. [CrossRef]
8. Dwivedi, A.; Kaiwart, R.; Varma, M.; Velaga, S.; Poswal, H. High-pressure structural investigations on $InPO_4$. *J. Solid State Chem.* **2020**, *282*, 121065. [CrossRef]
9. Butcher J., D.P.; Gewirth, A.A. Photoelectrochemical response of $TlVO_4$ and $InVO_4$: $TlVO_4$ composite. *Chem. Mater.* **2010**, *22*, 2555–2562. [CrossRef]
10. Zhao, C.; Tan, G.; Yang, W.; Xu, .; Liu, T.; Su, Y.; Ren, H.; Xia, A. Fast interfacial charge transfer in α-Fe_2O_3- $\delta C \delta$/$FeVO_4$-x+ δC x-δ bulk heterojunctions with controllable phase content. *Sci. Rep.* **2016**, *6*, 38603. [CrossRef]
11. Balamurugan, M.; Yun, G.; Ahn, K.S.; Kang, S.H. Revealing the beneficial effects of $FeVO_4$ nanoshell layer on the $BiVO_4$ inverse opal core layer for photoelectrochemical water oxidation. *J. Phys. Chem. C* **2017**, *121*, 7625–7634. [CrossRef]

12. Marberger, A.; Elsener, M.; Ferri, D.; Sagar, A.; Schermanz, K.; Krocher, O. Generation of NH_3 selective catalytic reduction active catalysts from decomposition of supported $FeVO_4$. *ACS Catal.* **2015**, *5*, 4180–4188. [CrossRef]
13. Yi, X.; Li, J.; Chen, Z.; Tok, A. Single-crystalline $InVO_4$ nanotubes by self-template-directed fabrication. *J. Am. Ceram. Soc.* **2010**, *93*, 596–600. [CrossRef]
14. Yu, Y.; Ju, P.; Zhang, D.; Han, X.; Yin, X.; Zheng, L.; Sun, C. Peroxidase-like activity of $FeVO_4$ nanobelts and its analytical application for optical detection of hydrogen peroxide. *Sens. Actuators B* **2016**, *233*, 162–172. [CrossRef]
15. López-Moreno, S.; Errandonea, D.; Pellicer-Porres, J.; Martínez-García, D.; Patwe, S.J.; Achary, S.N.; Tyagi, A.K.; Rodríguez-Hernández, P.; Muñoz, A.; Popescu, C. Stability of $FeVO_4$ under Pressure: An X-ray Diffraction and First-Principles Study. *Inorg. Chem.* **2018**, *57*, 7860–7876. [CrossRef]
16. Errandonea, D.; Gomis, O.; García-Domene, B.; Pellicer-Porres, J.; Katari, V.; Achary, S.N.; Tyagi, A.K.; Popescu, C. New polymorph of $InVO_4$: A high-pressure structure with six-coordinated vanadium. *Inorg. Chem.* **2013**, *52*, 12790–12798. [CrossRef] [PubMed]
17. Arisi, E.; Sánchez, S.; Leccabue, F.; Watts, B.; Bocelli, G.; Calderón, F.; Calestani, G.; Righi, L. Preparation and characterization of $AlVO_4$ compound. *J. Mater. Sci.* **2004**, *39*, 2107–2111. [CrossRef]
18. Muller, J.; Joubert, J. Synthese sous haute pression d'oxygene d'une forme dense ordonne´ e de $FeVO_4$ et mise en evidence d'une varie´ te´ allotropique de structure $CrVO_4$. *J. Solid State Chem.* **1975**, *14*, 8–13. [CrossRef]
19. Oka, Y.; Yao, T.; Yamamoto, N.; Ueda, Y.; Kawasaki, S.; Azuma, M.; Takano, M. Hydrothermal synthesis, crystal structure, and magnetic properties of $FeVO_4$-II. *J. Solid State Chem.* **1996**, *123*, 54–59. [CrossRef]
20. Gonzalez-Platas, J.; López-Moreno, S.; Bandiello, E.; Bettinelli, M.; Errandonea, D. Precise characterization of the rich structural landscape induced by pressure in multifunctional $FeVO_4$. *Inorg. Chem.* **2020**, *59*, 6623–6630. [CrossRef]
21. Young, A.; Schwartz, C. High pressure forms of $CrVO_4$ and $FeVO_4$. *Acta Crystallogr. Sect. A Found. Crystallogr.* **1962**, *15*, 1305–1305. [CrossRef]
22. Laves, F.; Young, A.P.; Schwartz, C.M. On the high-pressure form of $FeVO_4$. *Acta Cryst.* **1964**, *17*, 1476–1477. [CrossRef]
23. Ouahrani, T.; Garg, A.B.; Rao, R.; Rodríguez-Hernández, P.; Muñoz, A.; Badawi, M.; Errandonea, D. High-Pressure Properties of Wolframite-Type $ScNbO_4$. *J. Phys. Chem. C* **2022**, *126*, 4664–4676. [CrossRef]
24. Bader, R.F. Atoms in molecules. *Accounts Chem. Res.* **1985**, *18*, 9–15. [CrossRef]
25. Jones, R.O. Density functional theory: Its origins, rise to prominence, and future. *Rev. Mod. Phys.* **2015**, *87*, 897–923. [CrossRef]
26. Blöchl, P.E. Projector augmented-wave method. *Phys. Rev. B* **1994**, *50*, 17953–17979. [CrossRef] [PubMed]
27. Kresse, G.; Joubert, D. From ultrasoft pseudopotentials to the projector augmented-wave method. *Phys. Rev. B* **1999**, *59*, 1758–1775. [CrossRef]
28. Kresse, G.; Hafner, J. Ab initio molecular dynamics for liquid metals. *Phys. Rev. B* **1993**, *47*, 558–561. [CrossRef]
29. Kresse, G.; Hafner, J. Ab initio molecular-dynamics simulation of the liquid-metal–amorphous-semiconductor transition in germanium. *Phys. Rev. B* **1994**, *49*, 14251–14269. [CrossRef]
30. Kresse, G.; Furthmüller, J. Efficient iterative schemes for ab initio total-energy calculations using a plane-wave basis set. *Phys. Rev. B* **1996**, *54*, 11169–11186. [CrossRef]
31. Kresse, G.; Furthmüller, J. Efficiency of ab-initio total energy calculations for metals and semiconductors using a plane-wave basis set. *Comput. Mater. Sci.* **1996**, *6*, 15–50. [CrossRef]
32. Csonka, G.I.; Perdew, J.P.; Ruzsinszky, A.; Philipsen, P.H.T.; Lebègue, S.; Paier, J.; Vydrov, O.A.; Ángyán, J.G. Assessing the performance of recent density functionals for bulk solids. *Phys. Rev. B* **2009**, *79*, 155107. [CrossRef]
33. Dudarev, S.L.; Botton, G.A.; Savrasov, S.Y.; Humphreys, C.J.; Sutton, A.P. Electron-energy-loss spectra and the structural stability of nickel oxide: An LSDA+U study. *Phys. Rev. B* **1998**, *57*, 1505–1509. [CrossRef]
34. Ruiz-Fuertes, J.; Errandonea, D.; López-Moreno, S.; González, J.; Gomis, O.; Vilaplana, R.; Manjón, F.J.; Muñoz, A.; Rodríguez-Hernández, P.; Friedrich, A.; et al. High-pressure Raman spectroscopy and lattice-dynamics calculations on scintillating $MgWO_4$: Comparison with isomorphic compounds. *Phys. Rev. B* **2011**, *83*, 214112. [CrossRef]
35. López, S.; Romero, A.H.; Mejía-López, J.; Mazo-Zuluaga, J.; Restrepo, J. Structure and electronic properties of iron oxide clusters: A first-principles study. *Phys. Rev. B* **2009**, *80*, 085107. [CrossRef]
36. López-Moreno, S.; Romero, A.H.; Mejía-López, J.; Muñoz, A.; Roshchin, I.V. First-principles study of electronic, vibrational, elastic, and magnetic properties of FeF_2 as a function of pressure. *Phys. Rev. B* **2012**, *85*, 134110. https://doi.org/10.1103/PhysRevB.85.134110.
37. Mejía-López, J.; Mazo-Zuluaga, J.; López-Moreno, S.; Muñoz, F.; Duque, L.F.; Romero, A.H. Physical properties of quasi-one-dimensional MgO and Fe_3O_4-based nanostructures. *Phys. Rev. B* **2014**, *90*, 035411. [CrossRef]
38. Monkhorst, H.J.; Pack, J.D. Special points for Brillouin-zone integrations. *Phys. Rev. B* **1976**, *13*, 5188–5192. [CrossRef]
39. Parlinski, K. Computer Code PHONON. **2008**. Available online: http://wolf.ifj.edu.pl/phonon (accessed on 5 December 2022).
40. Romero-Vázquez, P.B.; López-Moreno, S.; Errandonea, D. First-principles study of $ATcO_4$ pertechnetates. *J. Phys. Chem. Solids* **2022**, *171*, 110979. [CrossRef]
41. Le Page, Y.; Saxe, P. Symmetry-general least-squares extraction of elastic data for strained materials from ab initio calculations of stress. *Phys. Rev. B* **2002**, *65*, 104104. [CrossRef]
42. Popelier, P.L.A. The QTAIM Perspective of Chemical Bonding. In *The Chemical Bond: Fundamental Aspects of Chemical Bonding*; John Wiley & Sons, Ltd: Hoboken, NJ, USA, 2014; chapter 8, pp. 271-308. [CrossRef]

43. Otero-de-la Roza, A.; Blanco, M.; Pendás, A.M.; Luaña, V. Critic: A new program for the topological analysis of solid-state electron densities. *Comput. Phys. Commun.* **2009**, *180*, 157–166. [CrossRef]
44. Otero-de-la Roza, A.; Johnson, E.R.; Luaña, V. Critic2: A program for real-space analysis of quantum chemical interactions in solids. *Comput. Phys. Commun.* **2014**, *185*, 1007–1018. [CrossRef]
45. Vega, D.; Almeida, D. AIM-UC: An application for QTAIM analysis. *J. Comput. Methods Sci. Eng.* **2014**, *14*, 131–136. [CrossRef]
46. Momma, K.; Izumi, F. VESTA3 for three-dimensional visualization of crystal, volumetric and morphology data. *J. Appl. Crystallog.* **2011**, *44*, 1272–1276. [CrossRef]
47. Birch, F. Finite elastic strain of cubic crystals. *Phys. Rev.* **1947**, *71*, 809–824. [CrossRef]
48. Touboul, M.; Ingrain, D. Syntheses et propriétés thermiques de $InVO_4$ et $TlVO_4$. *J. Less Common Met.* **1980**, *71*, 55–62. [CrossRef]
49. Hotta, Y.; Ueda, Y.; Nakayama, N.; Kosuge, K.; Kachi, S.; Shimada, M.; Koizumi, M. Pressure-products diagram of $FeVO_4$ system ($0 \leq x \leq 0.5$). *J. Solid State Chem.* **1984**, *55*, 314–319. [CrossRef]
50. Errandonea, D. High pressure crystal structures of orthovanadates and their properties. *J. Appl. Phys.* **2020**, *128*, 040903. [CrossRef]
51. Díaz-Anichtchenko, D.; Errandonea, D. Comparative Study of the Compressibility of $M_3V_2O_8$ (M = Cd, Zn, Mg, Ni) Orthovanadates. *Crystals* **2022**, *12*. [CrossRef]
52. Botella, P.; Errandonea, D.; Garg, A.; Rodriguez-Hernandez, P.; Muñoz, A.; Achary, S.; Vomiero, A. High-pressure characterization of the optical and electronic properties of $InVO_4$, $InNbO_4$, and $InTaO_4$. *SN Appl. Scien.* **2019**, *1*, 389. [CrossRef]
53. Monteseguro, V.; Ruiz-Fuertes, J.; Contreras-García, J.; Rodríguez-Hernández, P.; Muñoz, A.; Errandonea, D. High pressure theoretical and experimental analysis of the bandgap of $BaMoO_4$, $PbMoO_4$, and $CdMoO_4$. *Appl. Phys. Lett.* **2019**, *115*, 012102. [CrossRef]
54. Romero-Vázquez, P.B.; López-Moreno, S. Ab initio study of $RaWO_4$: Comparison with isoelectronic tungstates. *J. Solid State Chem.* **2023**, *317*, 123709. [CrossRef]
55. Nye, J.F.; et al. *Physical properties of crystals: their representation by tensors and matrices*; Oxford university press, 1985.
56. Mouhat, F.; Coudert, F.X. Necessary and sufficient elastic stability conditions in various crystal systems. *Phys. Rev. B* **2014**, *90*, 224104. [CrossRef]
57. ping Feng, L.; tang Liu, Z.; jun Liu, Q. Structural, elastic and mechanical properties of orthorhombic SrHfO3 under pressure from first-principles calculations. *Phys. B Condens. Matter* **2012**, *407*, 2009–2013. [CrossRef]
58. Najafvandzadeh, N.; López-Moreno, S.; Errandonea, D.; Pavone, P.; Draxl, C. First-principles study of elastic and thermal properties of scheelite-type molybdates and tungstates. *Mater. Today Commun.* **2020**, *24*, 101089. [CrossRef]
59. Voigt, W. *Lehrbuch Kristallphysik*; Springer: Berlin/Heidelberg, Germany, 1928. [CrossRef]
60. Reuss, A. Berechnung der Fliebgrenze von Mischkristallen auf Grund der Plastizitatsbedingung für Einkristalle . *Angew Appl. Math. Mech.* **1929**, *9*, 49–58. [CrossRef]
61. Tian, Y.; Xu, B.; Zhao, Z. Microscopic theory of hardness and design of novel superhard crystals. *Int. J. Refract. Met. Hard. Mater.* **2012**, *33*, 93–106. [CrossRef]
62. Singh, J.; Sahoo, S.S.; Venkatakrishnan, K.; Vaitheeswaran, G.; Errandonea, D. High-pressure study of the aurophilic topological Dirac material AuI. *J. Alloys Compd.* **2022**, *928*, 167178. [CrossRef]
63. Prawoto, Y. Seeing auxetic materials from the mechanics point of view: A structural review on the negative Poisson's ratio. *Comput. Mater. Sci.* **2012**, *58*, 140–153. [CrossRef]
64. Liu, Y.; Jia, D.; Zhou, Y.; Zhou, Y.; Zhao, J.; Li, Q.; Liu, B. Discovery of ABO4 scheelites with the extra low thermal conductivity through high-throughput calculations. *J. Mater.* **2020**, *6*, 702 – 711. [CrossRef]
65. Tvergaard, V.; Hutchinson, J.W. Microcracking in Ceramics Induced by Thermal Expansion or Elastic Anisotropy. *J. Am. Ceram. Soc.* **1988**, *71*, 157–166. [CrossRef]
66. Grimvall, G.; Magyari-Köpe, B.; Ozoliņš, V.; Persson, K.A. Lattice instabilities in metallic elements. *Rev. Mod. Phys.* **2012**, *84*, 945. [CrossRef]